Mismatch Analysis of DTCs With an Improved BIST-TDC in 28-nm CMOS

Peng Chen, *Member, IEEE*, Jun Yin, *Member, IEEE*, Feifei Zhang, *Student Member, IEEE*,
Pui-In Mak, *Fellow, IEEE*, Rui P. Martins, *Fellow, IEEE*,
and Robert Bogdan Staszewski, *Fellow, IEEE*

Abstract—Nonlinearity of a digital-to-time converter (DTC) is pivotal to spur performance in DTC-based all-digital phase-locked-loops (ADPLL). In this paper, we characterize and analyze the mismatch of cascaded-delay-unit DTCs. Through an improved built-in-self-test (BIST) time-to-digital converter (TDC) assisted with phase-to-frequency detector (PFD), a measurement system of sub-half-ps accuracy is constructed to conduct the characterization. Fabricated in 28-nm CMOS, the DTC transfer functions are measured, and mismatches are compared against Monte-Carlo simulation results. The integral nonlinearity (INL) results are compared against each other and converted to the in-band fractional spur level when the DTC would be deployed in the ADPLL. The BIST-TDC system thus characterizes the on-chip delays without expensive equipment or complex setup. The effectiveness of adding a PFD into the ΔΣ loop is validated. The entire BIST system consumes 0.6 mW with a system self-calibration algorithm to tackle the analog blocks' nonlinearities.

Index Terms—All-digital PLL (ADPLL), build-in self-test (BIST), digital-to-time converter (DTC), fractional spur, jitter, mismatch, noise shaping, phase/frequency detector (PFD), self calibration, time-to-digital converter (TDC).

I. INTRODUCTION

ALL-DIGITAL phase-locked loops (ADPLL) offer extensive re-configurability and require a small area for their (digital) loop filter in scaled CMOS [1]–[6]. A digital-to-time converter (DTC) is a critical block in fractional-N ADPLLs. In contrast to the voltage/current-domain operation of the conventional phase-detection circuitry, made up of a phase/frequency detector (PFD) and a charge pump, and suffering from the degraded dynamic range due to the reduced voltage headroom and stronger channel-length modulation in current mirrors, the time-domain quantization benefits from the steeper transition edges in the advanced technology nodes [2]. Consequently, the time-domain converters promise faster phase detection speeds and lower power consumption at lower supply voltages [6]–[9].

As shown in Fig. 1(a), the DTC, whose mismatch is the main investigation target of this work, is placed in the reference signal path in front of the time-to-digital converter (TDC) [5]. The DTC's nonlinearity is directly reflected in the ADPLL output spectrum, producing in-band fractional spurs which, by definition, cannot be suppressed by the loop filter. Thus, DTC architectures with better linearity, such as using a constant-slope technique [8], [10], are being explored. Since the DTC works periodically and is controlled by the accumulated fractional control word, FCW_frac, its nonlinearity and the in-band spur level have a mathematical relationship. We confine the study of this relationship to the ADPLL architecture shown in Fig. 1(a). We assume the nonlinearity forms a pure sinusoidal shape covering the whole period of the digitally controlled oscillator (DCO), T_{DCO}, with an amplitude of A_{nonl}, where A_{nonl} is normalized to one oscillator period. Then, the spur level can be expressed as [11]:

$$\mathcal{L} = 20 \cdot \log_{10}(\pi A_{nonl}). \qquad (1)$$

That relationship is plotted in Fig. 1(b). It can be observed that if a -40 dBc in-band fractional spur is desired, the nonlinearity amplitude should satisfy $A_{nonl} < 0.32\%$. Note that in this specific example, INL (normalized to LSB) and the nonlinearity amplitude are related by

$$A_{nonl} = \frac{INL \cdot \Delta_{DTC}}{T_{DCO}}, \qquad (2)$$

where Δ_{DTC} is the DTC resolution. Delay-cascading DTCs are attractive due to their simple implementation and acceptable
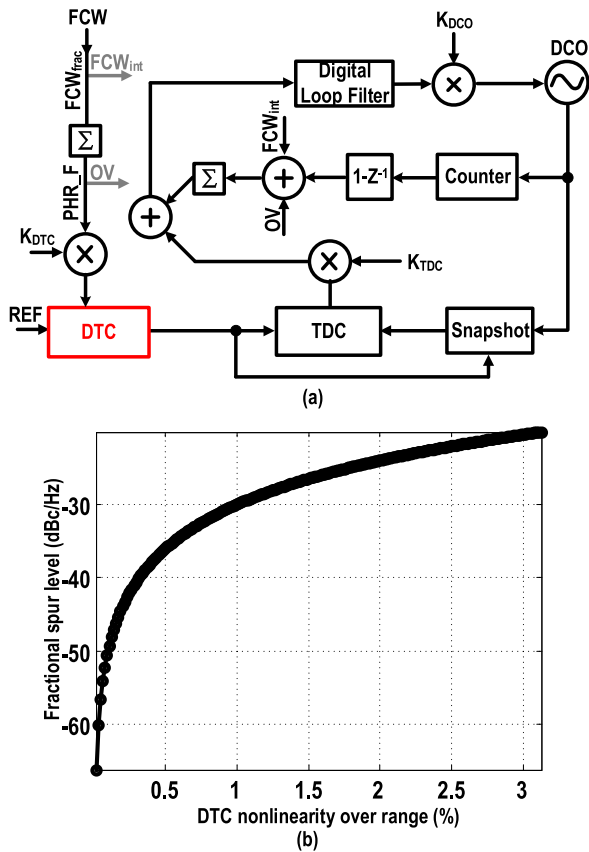
Fig. 1. (a) DTC-assisted ADPLL with DTC located in the reference path. (b) Influence of DTC nonlinearity (normalized to the DCO period) on the ADPLL's in-band fractional spurs.

unit stage delay [3], [6], [12]. Their nonlinearity is dominated by device mismatches, which can be optimized through proper device sizing and symmetrical layout. In practice, they can support the $\leq 0.3\%$ peak INL harmonic amplitude to guarantee the < -40 dBc in-band fractional spurs [3], [5], [12]. A phase rotation technique can be further applied to reduce the DTC's nonlinearity influence by restricting the effective DTC range to a smaller portion of T_{DCO} [7]. Two delay-cascading DTC architectures adopted in the previous ADPLLs [6], [12] are analyzed in this work. Although fabricated with different transistor sizes and even in different technologies, the measurement results are normalized and compared.

To perform an on-chip delay characterization, namely measuring the DTC transfer function, TDCs are widely used [13]–[22]. In general, the "measurement system" should push its precision one order of magnitude finer than the DTC resolution under test. In our case, the TDC resolution should be at the level of 1 ps, or even finer. This basic requirement excludes the flash TDCs whose resolution is at the gate delay level [13]. The vernier TDCs [14], [15] can achieve the sub-gate resolution but they suffer from large mismatches between the fast and slow paths, and that requires a non-trivial calibration for each delay stage. The ADC-based TDCs can provide the desired resolution with reasonable linearity [16], [17]. However, the covered delay range is limited. Increasing the range while keeping the same resolution will

inevitably sacrifice the linearity, which still needs to be calibrated. The $\Delta\Sigma$ or noise shaping TDCs [18]–[28] can relax the range-linearity trade-off. Unfortunately, their gain changes over PVT variations, which is normally calibrated by an on-chip PLL. In conclusion, the conventional TDC architectures, when employed to measure the DTC transfer function, require complex and expensive lab equipment or extra on-chip circuitry to calibrate the gain and mismatch of the TDC itself.

To overcome the aforementioned drawbacks, we have previously proposed to wrap-around the DTC in a loop of low hardware complexity, creating a 1st-order $\Delta\Sigma$ TDC [1], [29]. A system self-calibration algorithm was utilized for non-ideal analog effects. To verify the DTC mismatch analysis with a highly accurate measurement, this work improves the precision of the BIST $\Delta\Sigma$-TDC by reducing the charge pump noise by means of an additional PFD. The system noise contributions are analyzed to verify the proposed technique.

In addition to the targeted ADPLL application, the proposed BIST-TDC can also be used for characterizing the gain of other TDCs or to replace the digital delay-locked loop in outphasing transmitters [30].

This paper is organized as follows. Mismatches of three popular DTC architectures are analyzed in Section II. Section III describes the improved BIST $\Delta\Sigma$-TDC. Measurement results are presented and discussed in Section IV.

II. ANALYSIS OF DTC MISMATCHES

In addition to the two separate DTC architectures suitable for an ADPLL, a third DTC architecture with around 100 fs resolution is also implemented. It explores the vernier concept applied to the DTC design by means of MOS capacitance matching. Every DTC is made up of cascading 32 delay units in a chain targeting 5-bit performance. Mismatches between delay units will be investigated in this section.

A. DTC #1: Selector-Based DTC

Shown in Fig. 2, the first DTC was originally proposed in [6] and deployed in the first-ever sub-1 mW ultra-low-power ADPLL. The ADPLL architecture is similar to that in Fig. 1(a), yielding the same in-band fractional spur sensitivity to the DTC nonlinearity. The top part of Fig. 2 shows the DTC block diagram. Extra delay units are placed at each side of the delay chain. Acting as dummies, they are intended to retain the first and last cells' loading similar to that in other delay units. Every delay unit needs two delay control codes: EK for selecting the clock feeder (M_5–M_9) and EN for enabling the delay element (M_{10}–M_{17}). The input signal first goes through only one clock feeder controlled by EK. Then, it propagates through the remaining delay stages towards the output port. Therefore, the delay elements after the selected clock feeder are enabled through EN $= 0$, while the delay elements placed in front of the selected clock feeder are disabled through EN $= 1$. The disabled delay elements provide a high output impedance to the acting transition edges. Consequently, they do not affect the transition timing of the input's critical edge.
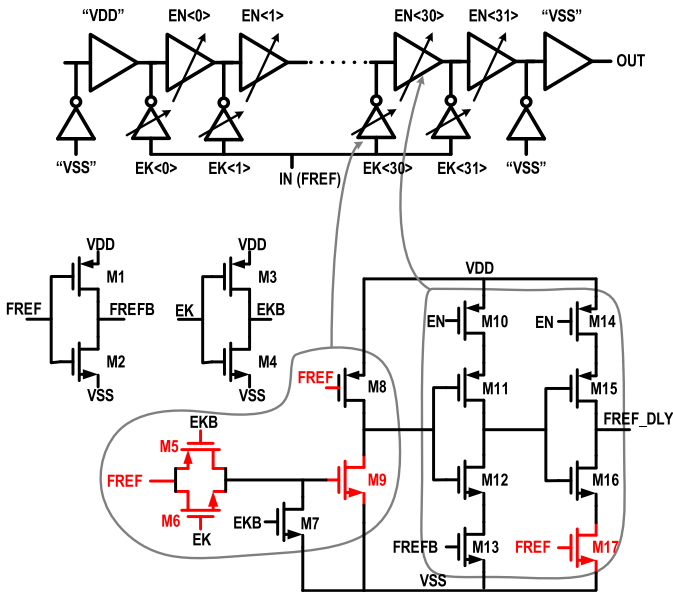
Fig. 2.   DTC #1 (based on [6]): schematic.

Fig. 3.   DTC #1: Monte-Carlo simulation results with 200 run times.

Fig. 4.   DTC #2: schematic with EK driven by DCW inverters.

Extracted from the measurement results [1], [6], this DTC's transfer function of delay versus digital control word (DCW) manifests non-monotonicity. Considering its delay-cascading structure, it is unexpected to observe that choosing the shorter path may yield a longer delay. For example, the signal going through the clock feeder selected by EK⟨30⟩ can reach the OUT node earlier than the signal going through the path selected by EK⟨31⟩. This phenomenon has not been clearly explained in the previous publications but will be addressed in this section with the help of dedicated Monte-Carlo simulations.

As discussed in [1], when the input signal's (FREF) rising edge is the critical edge to be delayed, the clock feeder reverses it to the falling edge to propagate it through the delay elements. Therefore, the size for M_9 should be large enough in order to suppress the transistor noise. However, its gate capacitance is driven by the input signal, posing more pressure on the input buffer's driving capability. The devices/wires marked in red color are to be driven by FREF, causing the need for huge input buffers and symmetrical clock tree distribution for the FREF node. The rising time of FREF is still quite long. It was inferred in [1] that after the rising edge reaches the gate of M_{16}, M_{17} may not be fully enabled due to its huge size, which was intentionally designed to reduce the discharging on-resistance. This was an initial guess on the non-monotonicity. Monte-Carlo simulations based on the whole DTC chain are very time-consuming and do not make it easy to spot the main mismatch source. To remedy that, Monte-Carlo simulations are carried out in this work to focus on the selected delay unit. Figure 3 provides quantitative mismatch information with 'local-only' variations, and discovers the root cause which has not been identified before. Note that the delay is also affected by the input signal's transition characteristics and output loading. The same driver and loading are placed in the testbench of the characterized individually selected delay unit.
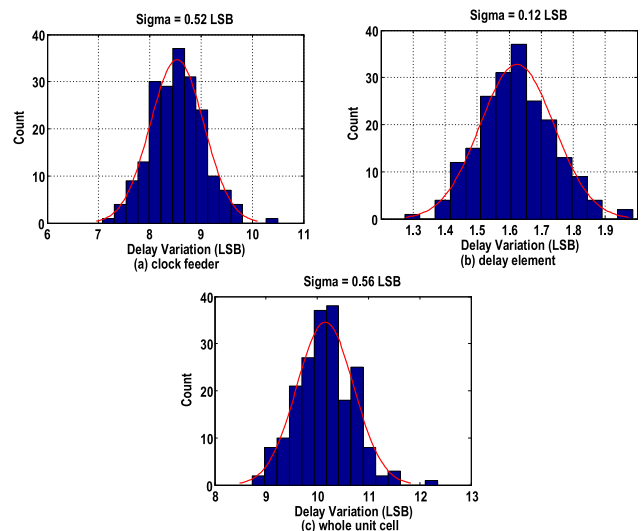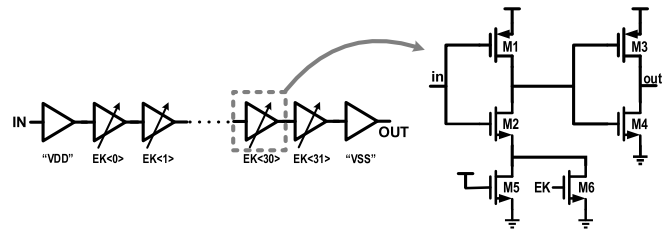
Figure 3 demonstrates the delay variations for the selected clock feeder, its corresponding delay element, and the whole delay unit. The active clock feeder contributes to the majority of the mismatches. The standard deviation of the clock feeder's delay is up to 0.52 LSB. As a comparison, the delay element merely contributes $\sigma = 0.12$ LSB. Furthermore, the delay element always presents a positive delay. Its mismatch does not intrinsically cause any non-monotonicity issues. In contrast, two neighboring clock feeders with a delay difference larger than one LSB end up with non-monotonicity, which is very likely to happen based on Fig. 3(a). It should be pointed out that the propagation time of the clock feeder is about $9\times$ of the DTC resolution, i.e. one order of magnitude higher. This DTC architecture demands the clock feeder to have a better mismatch performance than the delay element. However, the small sizes of $M_{5,6,7}$ are favored to reduce the input driver's loading. Enlarging their sizes will further increase the input signal's rising time. This design trade-off is hard to be balanced. Replacing the transmission gate with an *AND* gate can relax this trade-off by reducing the parasitic loading for the input driver.

B. DTC #2: Variable-Resistance Delay Line

Variable delay of the second DTC, shown in Fig. 4, is controlled by selecting an on-resistance in one discharging path. To align with the digital control interface, M_6 can be either enabled or disabled. M_5 is always on by fixing its gate voltage
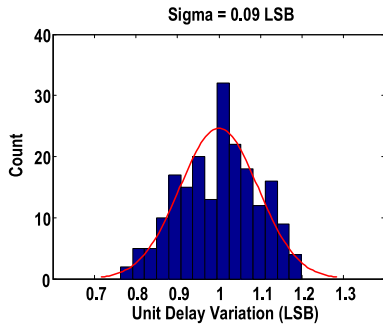
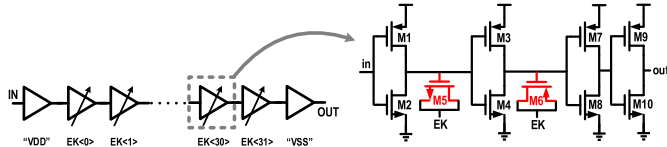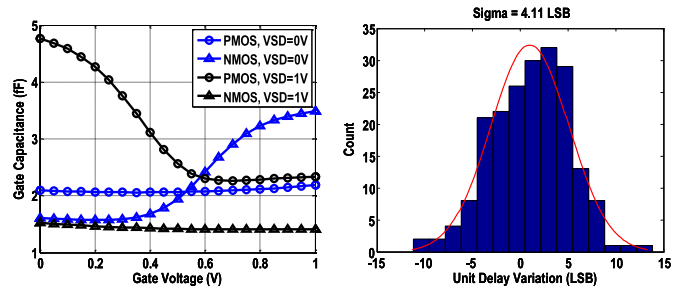Fig. 5. DTC #2: Monte-Carlo simulation results with 200 run times.

Fig. 6. DTC #3: schematic with EK driven by DCW inverters.

Fig. 7. DTC #3: (a) gate capacitance of the $M_{5,6}$ MOS capacitors versus their gate voltage under different control conditions of EK, and (b) Monte-Carlo simulation results with 200 run times.

to V_{DD}. Together with M_6, the two are connected in parallel in the first inverter's discharging path. The impedance seen from the M_2 source to ground is determined by the control signal EK. M_5's on-resistance dominates when M_6 is disabled. When EK $= 1$, the parallel on-resistance of M_5 and M_6 is significantly lower than when EK $= 0$. Extra delay units are inserted at the input and output ports of the DTC to reshape the transition edges and mimic the loading environment for the first (EK$\langle 0 \rangle$) and last (EK$\langle 31 \rangle$) core delay units.

The discharging time from the node of the first inverter's output, namely the second inverter's input, is different at various digital control codes. It can affect the second inverter's output transition time and shape, which will disturb the following delay unit. Thus, even though specific numbers of delay stages can be enabled randomly within this delay chain, the implemented selection always starts from the front ones. With the same input transition edges for the active cells, the delay mismatch is limited to the devices. Considering one delay unit, the capacitances, including the parasitics from the gate of $M_{3,4}$ and the drain of $M_{1,2,5,6}$, the source of M_2 and the interconnecting wires, should be discharged until reaching the threshold voltage of the second inverter. The transistors' capacitance and the parasitic capacitance can be optimized through a symmetrical layout. The on-resistance from $M_{2,5,6}$ is another source of mismatch, which also relies on the layout optimization. Large transistors' sizes burning more power can be traded for the better mismatch performance under the same resolution requirement. The Monte-Carlo simulation results shown in Fig. 5 demonstrate a much better standard deviation compared to DTC #1. One standard deviation is only 0.09 LSB from the schematic-level simulations.

C. DTC #3: "Vernier" DTC

Variable delay of the third DTC is realized through adjusting its capacitive loading difference. Its schematic is shown in Fig. 6. The MOS capacitors (M_5 and M_6) are put at the first and second inverters' output nodes. Two extra inverters are cascaded to isolate the variable capacitance loading from other delay units. Generally, the MOS capacitance experiences a large variation during the transition from the strong inversion region to the depletion region. M_5 is NMOS and M_6 is PMOS. The resolution is determined by the difference of these two capacitances, in a similar principle as in a vernier TDC, but using only a single path. This architecture is certainly not practical due to the sub-ps resolution heavily depending on the matching. That capacitance difference is even smaller than the parasitic capacitance. However, it is interesting to discover the extent of variations the measurement results can produce.

The MOS capacitance of M$_5$/M$_6$ against the gate voltage is plotted in Fig. 7(a) for different source/drain voltages. It is apparent that both NMOS and PMOS capacitors exhibit the largest and smallest gate capacitances when they are in the strong inversion and depletion regions, respectively. Since the gate voltage is bounded within 0 to 1 V, the accumulation region does not arise.

Taking the rising edge as the critical one, while initially only considering M_5, the discharging process experienced by M_5 corresponds to two different gate capacitance trajectories as Fig. 7(a) shows. The integrated influence when the gate voltage changes from 1 V to $V_{th,M3}$ yields two different discharging times, under the scenarios of VSD $= 0$ V and VSD $= 1$ V. $V_{th,M3}$ denotes the threshold voltage of PMOS M_3 which is around half V_{DD} in this case. The averaged capacitance of M_5 when VSD $= 0$ V is much larger than that when VSD $= 1$ V. In other words, EK $= 0$ can increase the unit delay. The critical edge turns into the rising edge for M_6. The integrated influence when its gate voltage increases from 0 V to $V_{th,M8}$ affects the unit stage delay. $V_{th,M8}$ represents the threshold voltage of M_8. As a comparison, the averaged capacitance of M_6 when VSD $= 0$ V is relatively flat and much smaller than the case when VSD $= 1$ V. Therefore, EK $= 0$ will speed up the unit delay if only M_6 is considered. These two MOS capacitors present an opposite influence on the unit delay, manifesting a finer resolution if they are combined. However, as Fig. 7(b) shows, one sigma of the delay variation is as large as 4.11 LSB. This architecture is therefore not very practical. On the other hand, the mismatches are amplified, which makes it easier for characterization and comparison.
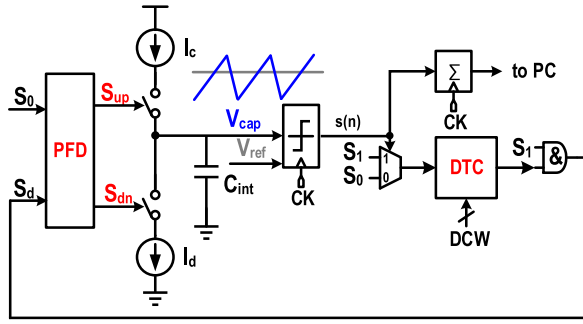
(a)
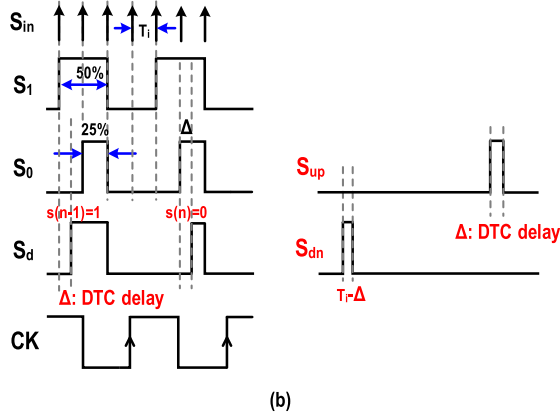
(b)

Fig. 8. Architecture of the improved first-order $\Delta\Sigma$ TDC: (a) top level block diagram, and (b) timing diagram.

III. IMPROVED FIRST-ORDER $\Delta\Sigma$ TDC

Following up on our previous work in [1], a PFD is inserted in front of the charge pump, as presented in the top level architecture in Fig. 8(a). The red labeled blocks highlight this work's implementation contributions: a PFD for the system-level improvement and DTCs for the block-level analysis.

The BIST-TDC is made up of the DTCs under test, a charge pump (CP), a clocked comparator, and the digital control logic. The timing diagram is illustrated in Fig. 8(b). The system needs one external input clock S_{in} with period T_i to normalize the DTC delay. Synthesized and auto-placed-and-routed dividers generate three low-frequency clocks, S_1, S_0, and CK. All frequencies of the generated clocks are one-quarter of the external input clock. S_1 has a 50% duty cycle while S_0 has a 25% duty cycle. Their falling edges are aligned. The comparator is driven by CK whose rising edge leads S_1 by one T_i. The loop works in such a way that the top plate voltage of the integration capacitor C_{int}, namely V_{cap}, toggles around the reference voltage V_{ref} which is connected to the negative input of the comparator. The possibility of '1' appearing in the comparator's '0/1' bit-stream maps the delay under test.

A. Operational Principle

Originally, S_0 directly controls the charge switch and S_d controls the discharge switch. S_0's duty cycle is constantly 25%, while S_d's pulsewidth ranges from 0% to 50%. When the loop parameters are properly selected, V_{cap} can stably
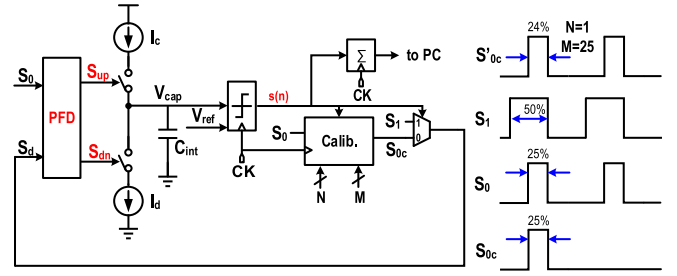

Fig. 9. System calibration scheme.

toggle around V_{ref} which is set here to 0.5 V. A more detailed mathematical explanation for the BIST-TDC working scheme can be found in [1].

It can be noticed that when S_0 and S_d are connected to the charge pump directly, there is a time window lasting T_i every cycle when charging and discharging paths are enabled at the same time. From the system point of view, those currents are wasted because the charging and discharging overlap time is fixed, containing no DTC delay information. Moreover, the current noise contributions from current sources I_c and I_d are added into V_{cap} during this unproductive time. With the help of PFD, the charging and discharging signals end up as S_{up} and S_{dn}. Therefore, shrunk pulses are applied on the charge pump without affecting the delay information under test. On the other hand, the added PFD will introduce extra jitter. However, this can be neglected compared to the optimized charge-pump noise.

B. System Self-Calibration

The system calibration scheme is shown in Fig. 9. The motivation is to remove influence of the non-ideal effects on the DTC transfer function. Major sources are the charging/ discharging current mismatch of the charge pump and the comparator offset. In the system calibration mode, the DTC under test is bypassed from the measurement path. A digital calibration block is inserted between S_0 and the MUX to help generate an equivalent delay by omitting some pulses from S_0 in response to the N and M inputs. For example, when $N = 1$ and $M = 25$, one pulse is omitted every 25 S_0 pulses. In such a way, the equivalent delay equals to $0.0385T_i$, or $N/(M + N)T_i$ expressed in a general way. The calibration block provides the equivalent delay with high precision due to all the edges of S_0 and S_1 being triggered by the rising edges of S_{in}. Note that the accuracy of the BIST-TDC in this work is assumed by the top-level mathematical constructs and has not been independently verified through direct (although extremely complicated laborious) measurements, such as [10], [31].

C. Noise Sources

In the calibration mode, the noise derives from the external high-speed clock, PFD, charge pump and comparator's thermal and flicker noises. In this improved version, the comparator is identical to that in [1]. Thus, only the noise of PFD and CP is investigated. Fig. 10 compares the noise with and without
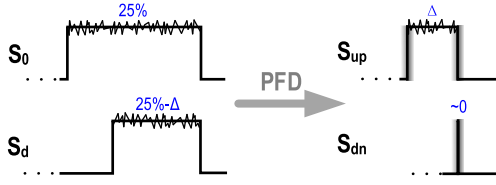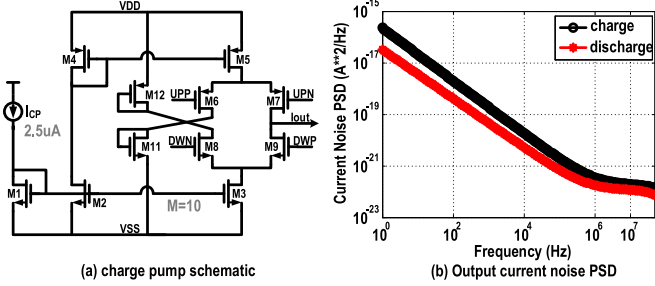
Fig. 10. Noise profiles w/ and w/o PFD.

Fig. 11. Charge pump: (a) schematic, and (b) PSD of the output current noise with 2.5 μA bias current.

Fig. 12. PFD: (a) schematic, (b) rms jitter spectrum, and (c) corresponding phase noise.

the PFD. Ignoring the external clock jitter, the transition edges of S_0 and S_1 are clean. The PFD applies timing variations to S_{up} and S_{dn}. In reality, S_{dn} still has a very short pulse with its pulsewidth determined by the PFD reset path delay. Therefore, the discharging path also suffers from the PFD jitter. Regarding the noise contributed by the charge pump, PFD significantly reduces the noise window, making the charge pump noise contribution less than half of the value in the case without PFD.

To quantify the charge pump's noise influence [32], [33], its output current noise simulation results are shown in Fig. 11(b), next to the current-steering charge pump schematic. Though the charge pump's power consumption cannot take advantage of adding a PFD, the same architecture is adopted for the noise comparison with the previous work [1]. S_{up} is connected to the UPP node and S_{dn} is connected to the DWP node. UPN and DWN are the inverted signals of UPP and DWP, respectively. The simulation results reveal that the charging current noise is larger than the discharging current because the current source M_5 encounters the double current mirroring from the external bias current source I_{CP}. The flicker noise corner is close to 1 MHz. Being clocked at 50 MHz, the integrated current noise amplitude from 1 Hz to 25 MHz is 84 nA for the discharging path and 122 nA for the charging path. We assume that the two noise sources are uncorrelated and take 8 pF for the integration capacitor. Without the PFD and the delay under test being zero ($\Delta = 0$ in Fig. 10), the maximal disturbance on V_{ref} can be calculated as:

$$\Delta V_{cap} = \frac{122\,\text{nA} \times 5\,\text{ns} + 84\,\text{nA} \times 5\,\text{ns}}{8\,\text{pF}} = 129\,\mu\text{V}. \quad (3)$$

5 ns is the period of the external clock S_{in}. The calculated voltage variation at the charge pump output can be 129 μV due to the charge pump noise.

The PFD schematic is shown in Fig. 12(a). A system reset signal is inserted into the PFD reset path with the OR gate. Extra delays are added in the reset path to avoid
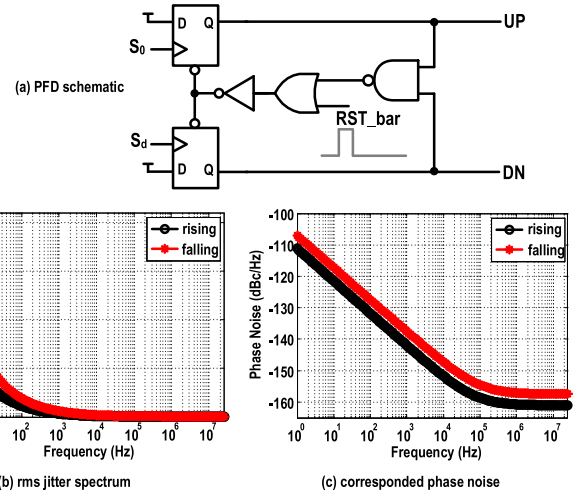
well known issues with the dead zone. The simulated rms jitter spectrum and corresponding phase noise are presented in Fig. 12(b) and (c) respectively. The flicker noise corner is around 100 kHz. The falling edge suffers from larger jitter due to the reset path. Circuits inside the PFD are selected from the standard cell library without optimizing for the jitter performance. Nevertheless, the added jitter is marginal [34], [35]. Integrating from 1 Hz to 25 MHz, the falling edge jitter is 311 fs and the rising edge jitter is 205 fs. Assuming for simplicity that the jitter of rising and falling edges is uncorrelated, their influences on V_{ref} can be calculated as:

$$\Delta V_{cap} = \frac{25\,\mu\text{A} \times 311\,\text{fs} + 25\,\mu\text{A} \times 205\,\text{fs}}{8\,\text{pF}} = 1.6\,\mu\text{V} \quad (4)$$

Compared to (3), the PFD induced jitter is deeply buried by the charge pump noise. Thus, it is worthwhile to introduce such a block into the BIST-TDC to improve the measurement precision.

D. Noise Improvement

To verify the above analysis, a behavioral model has been prepared. Simulations reveal that the $\Delta\Sigma$ loop can effectively suppress the white noise. For example, even though the external clock noise is modeled as 5 ps, the measurement precision can still be as fine as sub-100 fs if the noise is white. With the PFD, the charge pump's noise contribution is reduced, as shown in Fig. 13. However, the first-order $\Delta\Sigma$ loop suffers more from the flicker noise. Besides for the DTC under test, the flicker noise of charge pump and comparator dominates the flicker noise contributions of the analog blocks. To optimize the system noise performance, a longer channel length for the charge pump devices, especially for the current mirror, should be selected.

IV. MEASUREMENT RESULTS

Fabricated in 28 nm LP CMOS, the chip micrograph is shown in Fig. 14, together with the layout view. It occupies
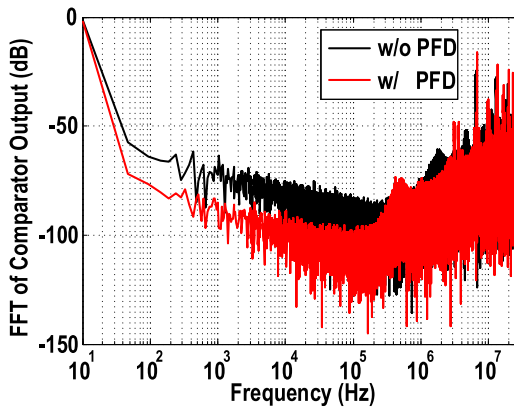
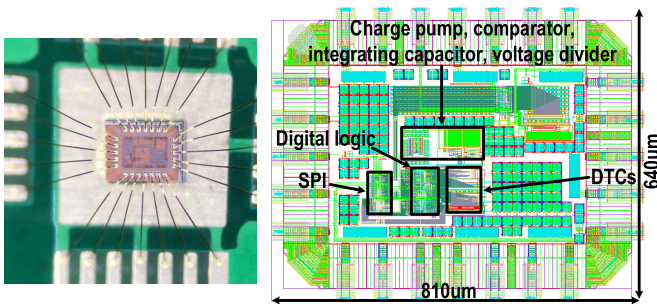Fig. 13. FFT spectrum of the comparator's output bitstream w/ and w/o PFD.

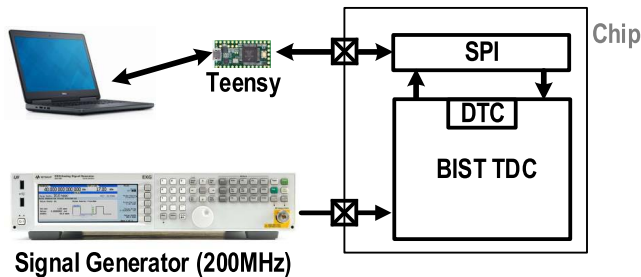Fig. 14. Chip micrograph and layout.

Fig. 15. Measurement setup.

810 μm × 640 μm of silicon area. The length of the bonding wire is around 1–1.5 mm. Thanks to the delay information being calculated on-chip and stored in the flip-flops, as well as to the input clock's thermal noise being filtered out by the $\Delta\Sigma$ loop, the package has limited influence on the measurement precision.

A. Experimental Setup

The measurement setup is illustrated in Fig. 15. A 200 MHz sine wave or square wave clock signal feeds into the chip. After a division by four, a 50 MHz clock is generated driving the BIST-TDC loop. The measured delay information is exported off-chip through a 1 MHz SPI interface for reporting purposes. All tests are completed *automatically* within several hours after setting up the measurement. The whole system power consumption is around 600 μW, similar to the one without the PFD [1]. It is limited by the
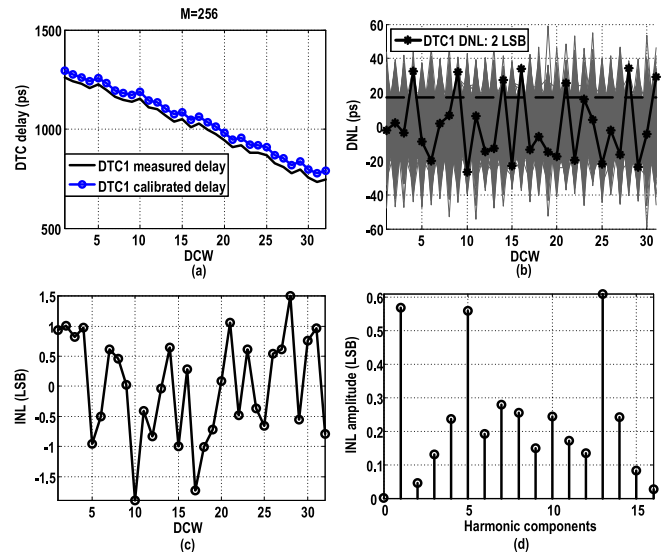

Fig. 16. DTC #1: (a) measured transfer function, (b) DNL, (c) INL, and (d) its harmonic components. Measured step-size (resolution) is 17 ps.

charge pump's current-steering structure, even though a shorter charging/discharging time is realized.

B. DTC Transfer Function and Mismatch

After processing the measured raw data, the DTC transfer function can be calculated. The DNLs are derived from the transfer function. Three DTCs are measured in order.

The transfer function of the first DTC is shown in Fig. 16(a). The system calibration adjusts the final delay information from the black curve to the blue curve. The delay range is 528 ps and LSB equals 17 ps. It is not surprising to observe the DNL jumping out of 1-LSB boundary, which is indicated by the dashed black line. Worst-case DNL is measured as large as 2.0 LSB. Standard deviation (σ) of a single-unit stage delay, 0.56 LSB, as shown in Fig. 3, is adopted to model the potential DNL performance. The DNL calculation is repeated 1000× and obeys the Gaussian distribution. The simulated results are shown in grey color in Fig. 16(b). It can be observed that the measured data matches quite well with the simulations. The simulated results indicate that the largest possible DNL can be even larger than 3 LSB. The calculated INL based on the best fit straight line is shown in Fig. 16(c).

To investigate how large in-band fractional spurs this DTC can induce, FFT is deployed to get the harmonic components' amplitude before applying formula (1) and (2). One more assumption is made here: the whole DTC range exactly covers one DCO period. The INL amplitudes for each harmonic are shown in Fig. 16(d). The 13th harmonic's amplitude is the highest one with a value of 0.61 LSB, corresponding to an in-band spur level of −24.5 dBc. This value is close to the one reported in [6]. In the BLE applications, the fractional spur located outside of the bandwidth can be suppressed through the loop. For high-performance ADPLLs, this DTC mismatch can be calibrated. As mentioned in Section II, the mismatch performance can be improved by replacing M_5, M_6, M_7 in Fig. 2 with an *AND* gate, as well as enlarging the channel

TABLE I
NONLINEARITY COMPARISON OF THE THREE DELAY-CASCADING DTCs

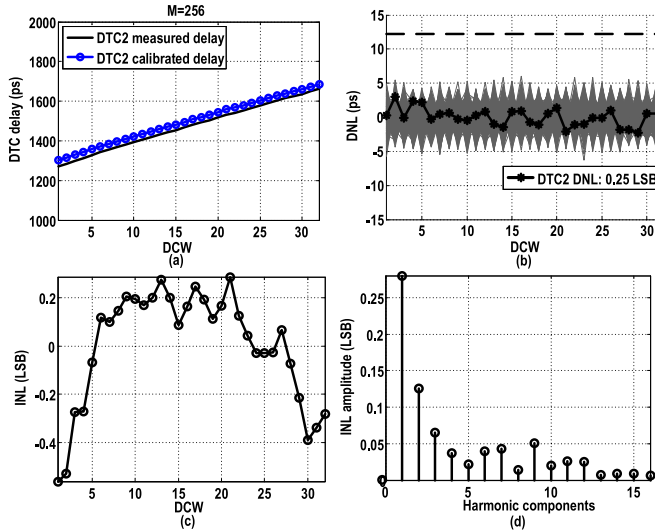|	DTC#1 sim.	DTC#1 meas.	DTC#2 sim.	DTC#2 meas.	DTC#3 sim.	DTC#3 meas.
DNL (LSB)	1.31	2.0	0.21	0.25	9.64	47.9
INL (LSB)	1.72	1.9	0.28	0.56	12.66	60.3

Fig. 17.   DTC #2: (a) measured transfer function, (b) DNL, (c) INL, and (d) its harmonic components. Measured step-size is 12 ps.

Fig. 18.   DTC #3: (a) measured transfer function and (b) DNL. Measured step-size is 89 fs.

Fig. 19.   (a) Histogram of measured DTCs. (b) Histogram of system self-calibration.

width of M_9. This architecture enjoys the potential small fixed offset delay but suffers mismatches from two sub-blocks: the delay element and clock feeder.

The measured performance of the second DTC is shown in Fig. 17. The delay range is 391 ps with 12 ps resolution. Its linearity is much better than the first one. The measured worst-case DNL is only 0.25 LSB, which matches with the 1000× repetitive simulations presented by the grey curves. Its INL is shown in Fig. 17(c). Possibly owing to the gradient of mismatch or doping, this INL curve is not 'friendly' to the fractional spurs. As Fig. 17(d) shows, the first harmonic component dominates. The highest harmonic amplitude of 0.28 LSB corresponds to −31.22 dBc of in-band fractional spur. This value can be optimized to <−40 dBc through larger device sizes, thus burning more power [12]. The gradient effects on the fractional spurs can be suppressed by enabling the delay units in a sequence of e.g. $1, N, 2, N − 1, \cdots$, rather than $1, 2, \cdots N$, where N is the number of delay units. Although this DTC has the best mismatch performance, its architecture is still sensitive to the supply noise and substrate noise, as well as suffering from PVT variations. To retain a stable performance, an LDO, deep N-well and proper guard-rings should be adopted.

Fig. 18 reports the measurement results of the third DTC. This clearly impractical DTC structure gives an overly nonlinear transfer function. It can only be observed that the delay tends to decline as the DCW increases. After least square fitting, one LSB is 89 fs. Although a 'fine' resolution is achieved, this architecture results in DNL of 47.9 LSB. Additionally, the measured DNL is much larger than the simulated

data, which is based on 4.1 LSB as 1σ for the unit delay. It indicates that for two different types of MOS capacitors' matching, the standard deviation can be much larger than the simulation results. That is also reasonable considering that hundreds of aF or one fF capacitance difference can be easily disturbed by the neighboring routing and dummy metal filling. Removing either M_5 or M_6 in Fig. 6, or controlling M_6 with the inverted version of EK could turn this DTC into a more practical architecture.

The nonlinearity performance of the three DTCs is summarized in Table I. Table II compares the proposed DTC measurement system with state-of-the-art found in the literature. The off-chip DTC measurement methods in [10], [31] offer a 'golden reference' for measuring the delay *difference*, although they cannot measure the absolute delay of DTC. Therefore, it appears that only the on-chip TDC arrangements are capable of characterizing a DTC under test with a fixed offset.

C. Measurement Precision

As discussed previously, the PFD can help with reducing the influence of the charge pump noise. The system is expected to provide better precision under the same conditions. Fig. 19 shows the histogram of the measured DTCs, together with the system self-calibration. The system self-calibration yields $\sigma = 0.47$ ps, a bit better than the previously reported

TABLE II
PERFORMANCE COMPARISON OF STATE-OF-THE-ART DTC DELAY MEASUREMENT SYSTEMS

	[10]	[31]	[13]	[19]	[23]	[25]	[1]	This work[1]
Method	off-chip freq. domain	off-chip oscilloscope	on-chip TDC	on-chip TDC	on-chip TDC	on-chip TDC	on-chip BIST-TDC	on-chip BIST-TDC
Technology (nm)	65	28	90	90	65	65	28	28
Precision (ps)	<0.01	<0.01	17	0.14/0.315	3.8	0.182	0.65	0.47
Calibration	No	No	Yes w. ADPLL	Yes off-chip	Yes off-chip	Yes w. ADPLL	Yes on-chip	Yes on-chip
Absolute delay	No	No	Yes	Yes	Yes	Yes	Yes	Yes
Conversion rate (MS/s)	NA	NA	26	0.1/1	2.5	1	3e-6	3e-6
Clock freq. (MHz)	NA	NA	26	250 s	205	250	50	50
Area(mm^2)	NA	NA	0.01	0.02	0.06	0.055	0.06	0.06
Power (mW)	NA	NA	1.8	1.5	0.63	8.4	0.6	0.6

[1] 200 MHz input clock, 2.5 μA charge pump bias current and 2^{24} running cycles are adopted in the above comparison.

value 0.65 ps [1]. This is likely due to the input clock now being fed into the synthesized digital block directly. The divided clocks at 50 MHz are heavily affected by other digital cells, especially some digital standard cells adopting the minimum allowed size, introducing significant flicker noise into the digital power supply. The comparator's flicker noise is another major low-frequency noise source, which is to be optimized by enlarging the input pairs' size.

V. CONCLUSION

This work characterizes and analyzes the mismatches of three delay-cascading DTCs, which have recently become very popular in digital PLLs. Through an improved built-in self-test (BIST)-TDC arrangement with an added PFD, the measurement results demonstrate a sub-half-ps precision in the system self-calibration mode. Fabricated in 28-nm CMOS, the DTC transfer functions are measured, and mismatches are compared against Monte-Carlo simulation results. The integral-nonlinearity (INL) information is translated to the in-band fractional spur level of digital PLLs. Noise contributions within the first-order $\Delta\Sigma$ loop are analyzed, proving the effectiveness of adding a PFD into the $\Delta\Sigma$ loop. The whole BIST system consumes 0.6 mW with a system self-calibration algorithm to tackle the nonlinearities of analog blocks.

ACKNOWLEDGMENT

The authors would like to thank TSMC University Shuttle for the chip fabrication, and Dr. Hsieh-Hung Hsieh (TSMC) and Dr. Teerachot Siriburanon for help with the tapeout.

REFERENCES

[1] P. Chen, X. Huang, Y. Chen, L. Wu, and R. B. Staszewski, "An on-chip self-characterization of a digital-to-time converter by embedding it in a first-order $\Delta\Sigma$ loop," *IEEE Trans. Circuits Syst. I, Reg. Papers*, vol. 65, no. 11, pp. 3734–3744, Nov. 2018.

[2] R. B. Staszewski *et al.*, "All-digital TX frequency synthesizer and discrete-time receiver for Bluetooth radio in 130-nm CMOS," *IEEE J. Solid-State Circuits*, vol. 39, no. 12, pp. 2278–2291, Dec. 2004.

[3] N. Pavlovic and J. Bergervoet, "A 5.3GHz digital-to-time-converter-based fractional-N all-digital PLL," in *IEEE Int. Solid-State Circuits Conf. (ISSCC) Dig. Tech. Papers*, Feb. 2011, pp. 54–56.

[4] D. Tasca, M. Zanuso, G. Marzin, S. Levantino, C. Samori, and A. Lacaita, "A 2.9-to-4.0 GHz fractional-N digital PLL with bang-bang phase detector and 560-fs$_{rms}$ integrated jitter at 4.5-mW power," *IEEE J. Solid-State Circuits*, vol. 46, no. 12, pp. 2745–2758, Dec. 2011.

[5] Y. Wu, M. Shahmohammadi, Y. Chen, P. Lu, and R. B. Staszewski, "A 3.5–6.8-GHz wide-bandwidth DTC-assisted fractional-N all-digital PLL with a MASH $\Delta\Sigma$-TDC for low in-band phase noise," *IEEE J. Solid State Circuits*, vol. 52, no. 7, pp. 1885–1903, Jul. 2017.

[6] V. K. Chillara *et al.*, "9.8 An 860 μW 2.1-to-2.7GHz all-digital PLL-based frequency modulator with a DTC-assisted snapshot TDC for WPAN (Bluetooth smart and ZigBee) applications," in *IEEE Int. Solid-State Circuits Conf. (ISSCC) Dig. Tech. Papers*, Feb. 2014, pp. 172–173.

[7] Y.-H. Liu *et al.*, "An ultra-low power 1.7-2.7 GHz fractional-N sub-sampling digital frequency synthesizer and modulator for IoT applications in 40 nm CMOS," *IEEE Trans. Circuits Syst. I, Reg. Papers*, vol. 64, no. 5, pp. 1094–1105, May 2017.

[8] P. Chen, F. Zhang, Z. Zong, S. Hu, T. Siriburanon, and R. B. Staszewski, "A 31-μW 148-fs step 9-bit capacitor-DAC-based constant-slope digital-to-time converter in 28-nm CMOS," *IEEE J. Solid-State Circuits*, vol. 54, no. 11, pp. 3075–3085, Nov. 2019.

[9] S. Hu *et al.*, "A type-II phase-tracking receiver," *IEEE J. Solid-State Circuits*, vol. 56, no. 2, pp. 427–439, Feb. 2021.

[10] C. Palattella, E. Klumperink, Z. Ru, and B. Nauta, "A sensitive method to measure the integral nonlinearity of a digital-to-time converter, based on phase modulation," *IEEE Trans. Circuits Syst. II, Exp. Briefs*, vol. 62, no. 8, pp. 741–745, Aug. 2015.

[11] P. Chen, X. Huang, and R. B. Staszewski, "Spur suppression in all-digital phase-locked loops," in *Proc. IEEE Int. Symp. Circuits Syst. (ISCAS)*, May 2015, pp. 2565–2568.

[12] Z. Zong, P. Chen, and R. B. Staszewski, "A low-noise fractional-N digital frequency synthesizer with implicit frequency tripling for mm-wave applications," *IEEE J. Solid-State Circuits*, vol. 54, no. 3, pp. 755–767, Mar. 2019.

[13] R. B. Staszewski, S. Vemulapalli, P. Vallur, J. Wallberg, and P. T. Balsara, "1.3 V 20 ps time-to-digital converter for frequency synthesis in 90-nm CMOS," *IEEE Trans. Circuits Syst. II, Exp. Briefs*, vol. 53, no. 3, pp. 220–224, Mar. 2006.

[14] P. Dudek, S. Szczepanski, and J. V. Hatfield, "A high-resolution CMOS time-to-digital converter utilizing a Vernier delay line," *IEEE J. Solid-State Circuits*, vol. 35, no. 2, pp. 240–247, Feb. 2000.

[15] Y. Kim and T. W. Kim, "An 11 b 7 ps resolution two-step time-to-digital converter with 3-D Vernier space," *IEEE Trans. Circuits Syst. I, Reg. Papers*, vol. 61, no. 8, pp. 2326–2336, Aug. 2014.

[16] Z. Xu, S. Lee, M. Miyahara, and A. Matsuzawa, "A 0.84 ps-LSB 2.47 mW time-to-digital converter using charge pump and SAR-ADC," in *Proc. IEEE Custom Integr. Circuits Conf. (CICC) Dig. Papers*, Sep. 2013, pp. 1–4.

[17] A. Sai, S. Kondo, T. T. Ta, H. Okuni, M. Furuta, and T. Itakura, "19.7 A 65nm CMOS ADPLL with 360μW 1.6ps-INL SS-ADC-based period-detection-free TDC," in *Proc. IEEE Int. Solid-State Circuits Conf. (ISSCC)*, Jan. 2016, pp. 336–337.

[18] M. Gande, N. Maghari, T. Oh, and U. K. Moon, "A 71dB dynamic range third-order $\Delta\Sigma$ TDC using charge-pump," in *Proc. IEEE Symp. VLSI Circuits (VLSIC)*, Jun. 2012, pp. 168–169.

[19] A. Elshazly, S. Rao, B. Young, and P. K. Hanumolu, "A noise-shaping time-to-digital converter using switched-ring oscillators—Analysis, design, and measurement techniques," *IEEE J. Solid-State Circuits*, vol. 49, no. 5, pp. 1184–1197, May 2014.

[20] C. M. Hsu, M. Z. Straayer, and M. H. Perrott, "A low-noise wide-BW 3.6-GHz digital ΔΣ fractional-N frequency synthesizer with a noise-shaping time-to-digital converter and quantization noise cancellation," *IEEE J. Solid-State Circuits*, vol. 43, no. 12, pp. 2776–2786, Dec. 2008.

[21] F. Brandonisio and F. Maloberti, "An all-digital PLL with a first order noise shaping time-to-digital converter," in *Proc. IEEE Int. Symp. Circuits Syst. (ISCAS)*, May 2010, pp. 241–244.

[22] W. Yu, K. Kim, and S. Cho, "A 148 fs_{rms} integrated noise 4 MHz bandwidth second-order ΔΣ time-to-digital converter with gated switched-ring oscillator," *IEEE Trans. Circuits Syst. I, Reg. Papers*, vol. 61, no. 8, pp. 2281–2289, Aug. 2014.

[23] S. T. Chandrasekaran, A. Jayaraj, M. Danesh, and A. Sanyal, "A highly digital second-order oversampling TDC," *IEEE Solid-State Circuits Lett.*, vol. 1, no. 5, pp. 114–117, May 2018.

[24] F. Yuan and P. Parekh, "Analysis and design of an all-digital ΔΣ TDC via time-mode signal processing," *IEEE Trans. Circuits Syst. II, Exp. Briefs*, vol. 67, no. 6, pp. 994–998, Jun. 2020.

[25] M. B. Dayanik and M. P. Flynn, "Digital fractional-N PLLs based on a continuous-time third-order noise-shaping time-to-digital converter for a 240-GHz FMCW radar system," *IEEE J. Solid-State Circuits*, vol. 53, no. 6, pp. 1719–1730, Jun. 2018.

[26] Z. Huang and H. C. Luong, "An 82–107.6-GHz integer-N ADPLL employing a DCO with split transformer and dual-path switched-capacitor ladder and a clock-skew-sampling delta–sigma TDC," *IEEE J. Solid-State Circuits*, vol. 54, no. 2, pp. 358–367, Feb. 2019.

[27] W. Yu, K. Kim, and S. Cho, "A 0.22 ps rms integrated noise 15 MHz bandwidth fourth-order ΔΣ time-to-digital converter using time-domain error-feedback filter," *IEEE J. Solid-State Circuits*, vol. 50, no. 5, pp. 1251–1262, May 2015.

[28] Y. Wu, P. Lu, and R. B. Staszewski, "A 103 fs_{rms} 1.32mW 50MS/s 1.25MHz bandwidth two-step flash-ΔΣ time-to-digital converter for ADPLL," in *Proc. IEEE Radio Freq. Integr. Circuits Symp. (RFIC)*, Jun. 2015, pp. 95–98.

[29] P. Chen et al., "Design and built-in characterization of digital-to-time converters for ultra-low power ADPLLs," in *Proc. IEEE Eur. Solid-State Circuits Conf. (ESSCIRC)*, Sep. 2015, pp. 283–286.

[30] A. Ravi et al., "A 2.4-GHz 20-40-MHz channel WLAN digital out-phasing transmitter utilizing a delay-based wideband phase modulator in 32-nm CMOS," *IEEE J. Solid-State Circuits*, vol. 47, no. 12, pp. 3184–3196, Feb. 2012.

[31] S. Sievert et al., "A 2 GHz 244 fs-resolution 1.2 ps-peak-INL edge interpolator-based digital-to-time converter in 28 nm CMOS," *IEEE J. Solid-State Circuits*, vol. 51, no. 12, pp. 2992–3004, Dec. 2016.

[32] M. Leoncini, A. Bonfanti, S. Levantino, and A. L. Lacaita, "Efficient behavioral simulation of charge-pump phase-locked loops," *IEEE Trans. Circuits Syst. I, Reg. Papers*, vol. 65, no. 6, pp. 1968–1980, Jun. 2018.

[33] F. Herzel, S. A. Osmany, and J. C. Scheytt, "Analytical phase-noise modeling and charge pump optimization for fractional-N PLLs," *IEEE Trans. Circuits Syst. I, Reg. Papers*, vol. 57, no. 8, pp. 1914–1924, Aug. 2010.

[34] A. Homayoun and B. Razavi, "Analysis of phase noise in phase/frequency detectors," *IEEE Trans. Circuits Syst. I, Reg. Papers*, vol. 60, no. 3, pp. 529–539, Mar. 2013.

[35] K. Kundert, "Predicting the phase noise and jitter of PLL-based frequency synthesize," in *Phase-Locking High-Performance Systems: From Devices to Architectures*, Aug. 2003, pp. 46–69.

Peng Chen (Member, IEEE) received the B.Sc. degree in electronics from Huazhong University of Science and Technology, Wuhan, China, in 2012, the M.Sc. degree in microelectronic from Delft University of Technology (TU Delft), Delft, The Netherlands, in 2014, and the Ph.D. degree from University College Dublin in 2019.

From 2014 to 2015, he worked as a Test Manager with Huawei Technologies, Amsterdam. From 2017 to 2018, he was a Visiting Research Assistant with the University of Macau. From 2019 to 2021, he was a Post-Doctoral Researcher with Lund University. He is currently with Wuxi Grandmicro, China. His M.Sc. thesis was done at the IMEC Holst Center, Eindhoven, The Netherlands. His research interests include time domain data converters, frequency synthesizers, and wideband receiver.

Jun Yin (Member, IEEE) received the B.Sc. and M.Sc. degrees in microelectronics from Peking University, Beijing, China, in 2004 and 2007, respectively, and the Ph.D. degree in electronic and computer engineering from The Hong Kong University of Science and Technology (HKUST), Hong Kong, in 2013. He is currently an Associate Professor with the State Key Laboratory of Analog and Mixed-Signal VLSI, University of Macau (UM), Macau. His research interests include the CMOS RF integrated circuits for wireless communications and wireless sensing systems, specializing in the frequency generation and synthesis circuits, including oscillators, and PLLs.

Feifei Zhang (Student Member, IEEE) received the B.Sc. degree in navigation guidance and control from Beijing University of Aeronautics and Astronautics, the M.Sc. degree in microelectronics from Beijing Embedded System Key Laboratory, Beijing University of Technology, in 2014, and the Ph.D. degree from University College Dublin in 2021.

Her current research interest includes radio frequency digital-to-analog converters.

Pui-In Mak (Fellow, IEEE) received the Ph.D. degree from the University of Macau (UM), Macau, in 2006.

He is currently a Full Professor with the ECE Department, Faculty of Science and Technology, UM, and the Associate Director (Research) of the Institute of Microelectronics, UM, and the State Key Laboratory of Analog and Mixed-Signal VLSI. His research interests include analog and radio-frequency (RF) circuits and systems for wireless and multidisciplinary innovations.

Dr. Mak has been inducting as the Overseas Expert of the Chinese Academy of Sciences since 2018. He has been a fellow of the U.K. Institution of Engineering and Technology (IET) for contributions to engineering research, education, and services since 2018, and he has also been a fellow of the IEEE for contributions to radio-frequency and analog circuits since 2019. He was a TPC member of A-SSCC from 2013 to 2016 and in 2019, ESSCIRC from 2016 to 2017, and ISSCC from 2017 to 2019. He was a member of Board-of-Governors of the IEEE Circuits and Systems Society from 2009 to 2011. He was the Chairman of the Distinguished Lecturer Program of the IEEE Circuits and Systems Society from 2018 to 2019. He (co)-received the DAC/ISSCC Student Paper Award in 2005, the CASS Outstanding Young Author Award in 2010, the National Scientific and Technological Progress Award in 2011, the Best Associate Editor of TCAS-II from 2012 to 2013, the A-SSCC Distinguished Design Award in 2015, and the ISSCC Silkroad Award in 2016. In 2005, he was decorated with the Honorary Title of Value for Scientific Merits by the Macau Government. He was the TPC Vice Co-Chair of ASP-DAC in 2016. His involvements with IEEE, including the IEEE TRANSACTIONS ON CIRCUITS AND SYSTEMS—I: REGULAR PAPERS from 2010 to 2011 and from 2014 to 2015, an Editorial Board Member of the IEEE Press from 2014 to 2016, a Senior Editor of the IEEE JOURNAL ON EMERGING AND SELECTED TOPICS IN CIRCUITS AND SYSTEMS from 2014 to 2015, and an Associate Editor of the IEEE JOURNAL OF SOLID-STATE CIRCUITS since 2018, the IEEE SOLID-STATE CIRCUITS LETTERS since 2017, and the IEEE TRANSACTIONS ON CIRCUITS AND SYSTEMS—II: EXPRESS BRIEFS (TCAS-II) from 2010 to 2013. He was a Distinguished Lecturer of the IEEE Circuits and Systems Society from 2014 to 2015 and the IEEE Solid-State Circuits Society from 2017 to 2018.

Rui P. Martins (Fellow, IEEE) was born in April 1957. He received the bachelor's, master's, Ph.D. degrees and the Habilitation degree for a Full Professorship in electrical engineering and computers from the Department of Electrical and Computer Engineering (DECE), Instituto Superior Técnico (IST), University of Lisbon, Portugal, in 1980, 1985, 1992, and 2001, respectively.

Since October 1980, he has been with the DECE/IST, University of Lisbon. Since October 1992, he has been on leave from the University of Lisbon, and with the DECE, Faculty of Science and Technology (FST), University of Macau (UM), Macau, China, where he has been the Chair-Professor since August 2013. In FST, he was the Dean from 1994 to1997 and has been a UM's Vice-Rector since September 1997. From September 2008 to August 2018, he was a vice-rector (research) and from September 2018 to August 2023, he was a vice-rector (global affairs). Within the scope of his teaching and research activities he has taught 21 bachelor's and master's courses, and in UM, he has supervised (or co-supervised) 47 theses; Ph.D. (26) and master's (21). He authored or coauthored eight books and 12 book chapters; 48 patents (38 USA, three Taiwan, and seven China); 628 papers in scientific journals (263) and in conference proceedings (365), and other 69 academic works, in a total of 765 publications. He created in 2003 the Analog and Mixed-Signal VLSI Research Laboratory, UM, elevated in January 2011 to the State Key Laboratory (SKLAB), China (the first in Engineering in Macau), being its Founding Director. He was the Founding Chair of UMTEC (UM Company) from January 2009 to March 2019, supporting the incubation and creation in 2018 of Digifluidic, the first UM spin-off, whose CEO is a SKLAB Ph.D. graduate. He was also a Co-Founder of Chipidea Microelectronics (Macau) [later Synopsys-Macau] in 2001 and 2002.

Prof. Rui Martins a member of IEEE CASS Fellow Evaluation Committee (2013, 2014, and 2018), the Chair (2019), and the Vice-Chair (2021 and 2022). He was the IEEE Nominating Committee of Division I Director (CASS/EDS/SSCS) (2014) and on the IEEE CASS Nominations Committee (2016–2017). He was the Founding Chair of IEEE Macau Section (2003–2005) and IEEE Macau Joint-Chapter on Circuits And Systems (CAS)/Communications (COM) (2005–2008) and the 2009 World Chapter of the Year of IEEE CAS Society (CASS); the General Chair IEEE Asia Pacific Conference on CAS—APCCAS'2008, the Vice-President (VP) Region 10 (Asia, Australia, and Pacific) (2009–2011), and the VP of World Regional Activities and Membership of IEEE CASS (2012–2013). He was an Associate-Editor of IEEE TRANSACTIONS ON CIRCUITS AND SYSTEMS—II: EXPRESS BRIEFS (2010–2013) and a nominated best associate editor (2012–2013). In addition, he was the General Chair of ACM/IEEE Asia South Pacific Design Automation Conference—ASP-DAC'2016, receiving the IEEE Council on Electronic Design Automation (CEDA) Outstanding Service Award in 2016 and the General Chair of the IEEE Asian Solid-State Circuits Conference—A-SSCC 2019. He was also the Vice-President (2005–2014) and President (2014–2017) of the Association of Portuguese Speaking Universities (AULP), and received two Macau Government decorations: the Medal of Professional Merit (Portuguese, 1999) and the Honorary Title of Value (Chinese, 2001). In July 2010, he was elected unanimously as a Corresponding Member of the Lisbon Academy of Sciences, being the only Portuguese Academician working and living in Asia.

Robert Bogdan Staszewski (Fellow, IEEE) was born in Bialystok, Poland. He received the B.Sc. *(summa cum laude)*, M.Sc., and Ph.D. degrees in electrical engineering from The University of Texas at Dallas, Richardson, TX, USA, in 1991, 1992, and 2002, respectively.

From 1991 to 1995, he was with Alcatel Network Systems, Richardson, Texas, involved in SONET cross-connect systems for fiber optics communications. He joined Texas Instruments Incorporated, Dallas, TX, USA, in 1995, where he was elected as a Distinguished Member of Technical Staff (limited to 2% of technical staff). From 1995 to 1999, he was engaged in advanced CMOS read channel development for hard disk drives. In 1999, he co-started the Digital RF Processor (DRP) group within Texas Instruments with a mission to invent new digitally intensive approaches to traditional RF functions for integrated radios in deeply-scaled CMOS technology. He was appointed as a CTO of the DRP Group from 2007 to 2009. In 2009, he joined Delft University of Technology, Delft, The Netherlands, where he currently holds a guest appointment of a Full Professor (*Antoni van Leeuwenhoek Hoogleraar*). Since 2014, he has been a Full Professor with University College Dublin (UCD), Dublin, Ireland. He is also a Co-Founder of a startup company, Equal1 Labs, with design centers located in Silicon Valley and Dublin, Ireland, aiming to produce single-chip CMOS quantum computers. He has authored or coauthored five books, seven book chapters, 140 journals and 210 conference publications, and holds 210 issued U.S. patents. His research interests include nanoscale CMOS architectures and circuits for frequency synthesizers, transmitters and receivers, and quantum computers.

Prof. Staszewski was a recipient of the 2012 IEEE Circuits and Systems Industrial Pioneer Award. In May 2019, he received the title of Professor from the President of the Republic of Poland. He was also the TPC Chair of the 2019 European Solid-State Circuits Conference (ESSCIRC), Krakow, Poland.